Physics of Fluids

Prediction of airway deformation effect on pulmonary air-particle dynamics: A numerical study

Cite as: Phys. Fluids **33**, 101906 (2021); https://doi.org/10.1063/5.0065309
Submitted: 31 July 2021 • Accepted: 30 September 2021 • Published Online: 21 October 2021

Jianan Zhao (赵嘉南), Yu Feng (冯宇), Kenichiro Koshiyama (越山顕一朗), et al.

Physics of Fluids ARTICLE scitation.org/journal/phf

Prediction of airway deformation effect on pulmonary air-particle dynamics: A numerical study

Cite as: Phys. Fluids **33**, 101906 (2021); doi: 10.1063/5.0065309
Submitted: 31 July 2021 · Accepted: 30 September 2021 ·
Published Online: 21 October 2021

Jianan Zhao (赵嘉南),[1] Yu Feng (冯宇),[1,a)] Kenichiro Koshiyama (越山顕一朗),[2] and Huimin Wu (吴惠敏)[3]

AFFILIATIONS

[1]School of Chemical Engineering, Oklahoma State University, Stillwater, Oklahoma 74078, USA
[2]Graduate School of Technology, Industrial and Social Sciences, Tokushima University, Tokushima 770-8506, Japan
[3]Department of Medicine, The University of Oklahoma College of Medicine, Oklahoma City, Oklahoma 73117, USA

[a)]Author to whom correspondence should be addressed: yu.feng@okstate.edu

ABSTRACT

Most existing whole lung models neglect the airway deformation kinematics and assume the lung airways are static. However, neglecting the airway deformation effect on pulmonary air-particle flow dynamics significantly limits the modeling capability under disease-specific lung conditions. Therefore, a novel elastic truncated whole-lung (TWL) modeling framework has been developed to simulate the disease-specific airway deformation kinematics simultaneously with pulmonary air-particle flow dynamics using one-way coupled Euler–Lagrange method plus the dynamic mesh method. Specifically, the deformation kinematics of the elastic TWL model was calibrated with clinical data and pulmonary function test results for both healthy lung and lungs with chronic obstructive pulmonary diseases (COPDs). The transport dynamics of spherical sub micrometer and micrometer particles were investigated. Results show that noticeable differences in air-particle flow predictions between static and elastic lung models can be found, which demonstrates the necessity to model airway deformation kinematics in whole-lung models. The elastic TWL model predicted lower deposition fraction in mouth-throat regions and higher deposition fraction in lower airways. The effect of disease-specific airway deformation kinematics on particle transport and deposition in the whole lung was investigated, with a focus on the targeted drug delivery efficiency in small airways from generation (G8) to alveoli as the designated lung sites for COPD treatment using inhalation therapy. Simulation results indicate that with the exacerbation of COPD disease conditions, the highest delivery efficiency of the inhaled drug particles decreases which indicates that delivering aerosolized medications to small airways to treat COPD is more challenging for patients with severe disease conditions.

I. INTRODUCTION

Chronic obstructive pulmonary disease (COPD) is the fourth leading cause of death in America, which causes severe breathing difficulty due to airway stiffening, loss of airway deformation capability, and airway blockage induced by inflammation. As the standard COPD treatment, inhalation of therapeutic nano-/micro-particles has illustrated a long-standing drug delivery barrier to achieving desired therapeutic outcomes,[1] i.e., only <25% of the drug particles can be delivered to the deeper lung with most of the particles depositing in the upper airway. To overcome such a barrier and increase the drug delivery efficiency from today's 25% to 90% to the deeper lung [generation 8 (G8) to alveoli] for the better therapeutic outcome and reduced side effects, it is imperative to understand the pulmonary air-particle flow dynamics and the interaction with physiologically realistic airway deformation kinematics on a disease-specific level. The COPD induced loss in airway deformation capability limits the delivery of inhaled therapeutic particles to the deeper lung, of which the underlying fluid dynamics has not been well understood, unfortunately. Although computational fluid-particle dynamics (CFPD) models,[2–4] i.e., Euler–Lagrange based virtual lung models, can capture the laminar-to-turbulence pulmonary airflows accurately and predict the trajectories of embedded particles, most existing CFPD studies shares the following two simplifications as the model deficiencies:[4–8]

(1) Pulmonary routes (i.e., computational flow domain) are incomplete in that they do not span from mouth to alveoli.
(2) Static airway wall position is assumed by neglecting physiologically realistic airway deformation kinematics.

As a result, the required numerical modeling capability to predict the drug delivery efficiency from G8 to alveoli with the influence of disease-specific airway deformation kinematics is not available.

Specifically, although CFPD models have been extensively validated and widely used for decades to investigate particle-laden airflow transport phenomena in human respiratory systems,[4–10] only a few studies simulated the transport and deposition using whole-lung models. This lack of study is mainly due to two reasons:

(1) Reconstruction of small airway geometries is difficult due to the insufficient resolutions of medical images.[11,12]
(2) The computational cost would increase exponentially as the deep lung region (up to alveoli) needs to be simulated.

Several recent studies were carried out to address these limitations by developing whole-lung models.[13–24] Existing whole-lung research efforts include: (1) using trumpet geometry or other simplified one-dimensional (1D) or two-dimensional (2D) pipelines to represent the whole tracheobronchial (TB) tree[15,17–22,24,25] and (2) extending 3D upper airways to deep lungs and conducting CFD studies by truncating airways and applying advanced coupled boundary conditions.[13,14,16,23,25–27] Specifically, Kolanjiyil and Kleinstreuer[20] developed a whole-lung airway model by combining a basic 3D mouth-to-trachea geometry with an exponentially expanding 1D conduit structure (3D-1D model), i.e., the trumpet model, as a computationally efficient but simplified whole-lung model. Multiple inhalation–exhalation profiles were achieved in the trumpet model by controlling the displacement of the bottom wall of the trumpet, which represents the motion of the diaphragm. Poorbahrami *et al.*[15] established a whole-lung model to estimate age-dependent particle dosimetry by coupling a CFD upper airway model with an adapted 1D-based trumpet model. In the 1D region, the diffusion and advection terms were used to consider the distal airway branching structure and inhaled air convection effect, respectively. Such a model enables the prediction of regional particle fate in the lungs by using a multi-domain method. There are also other whole-lung modeling efforts, which simplified small airways using 1D pipelines or 2D in-plane airway models instead of 3D geometries.[20,24] Although such 3D-1D or 3D-2D models require relatively low computational cost, the oversimplified peripheral lung geometry (i.e., from a specific generation to alveoli) disables the accurate prediction of air-particle flow dynamics in physiologically realistic computational airway domains. To address such deficiencies, static truncated whole-lung modeling strategies have been developed, which maintains the key anatomical features of the human respiratory systems as well as the optimized computational efficiencies. Specifically, Longest *et al.*[16,28] extended mouth-to-throat models to lobar bronchi coupled with Stochastic Individual Path (SIP) approximations of bronchioles to predict the deposition of aerosol emitted from the dry powder inhaler. Koullapis *et al.*[14] constructed a 3D deep lung model covering the 15 most distal lung generations to study the airflow patterns at quiet/deep breathing and the gravity effect on regional deposition. However, all the SIP models mentioned above neglected the airway deformation kinematics. The most recent SIP-type whole-lung model was developed by Si *et al.*[27] simulated the expansion and contraction movement of the alveoli simultaneously with the transport of the inhaled virus-laden droplets, which still did not integrate the airway deformation from the trachea to G17 or the glottis.

Although there are whole-lung modeling strategies summarized above, the "static" airway assumption limits the physiological realism of those existing whole-lung models and disables the disease-specific air-particle flow dynamics predictions. Specifically, lung diseases can alter lung deformation kinematics. Losses of lung expansion and contraction capability are commonly diagnosed in multiple obstructive lung diseases such as chronic obstructive pulmonary disease (COPD)[29,30] and emphysema.[31] Such loss can significantly limit the delivery of inhaled therapeutic particles in nanoscale and microscale to distal airways as the designated sites for treatment.[32] As a result, although most previous numerical studies provided reasonable simplified methods for studying the air-particle transport phenomena in the lung by neglecting the physiologically realistic airway deformation, it is necessary to recover the anisotropic airway deformation kinematics in numerical study to pave the way to the next-generation virtual lung model which can reflect more physiologically realistic and disease-specific lung conditions. Therefore, recovering the real-time disease-specific anisotropic lung deformation in a whole-lung model from mouth to alveoli is necessary to reflect the physiologically realistic disease lung conditions and its effect on the inhaled particle transport and deposition. Research efforts have been made to address the modeling deficiencies by developing models to capture the deformation in certain regions,[13,30,33–46] i.e., alveolar movement, bronchioles movement, trachea-to-bronchi movement, and uvula motion. There are still no whole-lung models that can integrate the deformation kinematics of both the glottis and the TB tree, including the alveoli, to describe the physiologically realistic and disease-specific airway motions. Such modeling deficiency leads to two key fundamental questions unanswered in pulmonary air-particle flow dynamics:

(1) What is the role of disease-specific airway deformation kinematics on pulmonary air-particle flow dynamics and particle deposition mechanisms?
(2) How to enhance the particle delivery efficiency to G8-to-alveoli regions by modulating particle size, with the influence of the disease-specific airway deformation kinematics?

To fill the knowledge gaps and address the modeling deficiencies mentioned above, this study has developed an elastic truncated whole-lung (TWL) model to simulate the inhaled particle transport simulation simultaneously with the transient anisotropic airway expansion and contraction in the entire tracheobronchial (TB) tree as well as the glottis motion. Novel contributions of the elastic TWL model include the following:

(1) The capability of modeling the anisotropic disease-specific airway deformation kinematics.
(2) The inclusion of five 3D airway paths representing 5 lung lobes.
(3) The integration of the elastic heterogeneous alveoli model.[50]

Using the elastic TWL model, three disease-specific airway deformation kinematics representing healthy lung and diseased lung at two different COPD stages are investigated in this study,[47] i.e., GOLD I—mild and GOLD III—severe, were calibrated and simulated. The impacts of particle size and disease-specific airway deformations were investigated on the pulmonary airflow patterns and the resultant particle transport and deposition. Particle sizes of 0.1, 0.2, 0.5, 1.0, 2.0, 5.0, and 10.0 μm were modeled, representing the particle size range of aerosolized drug particles for inhalation therapy.[48] The objective of

this study is to (1) quantify how the changes in real-time airway deformation kinematics alter the pulmonary airflow features (i.e., laminar-to-turbulence transition and relaminarization) and particle distribution, thereby influencing the particle trajectories and deposition sites in the lung and (2) evaluate the modulated particle size to overcome the significant drug loss due to the upper airway deposition caused by turbulence dispersion, inertial impaction, and an interception with the moving airway boundaries, thereby enhancing the particle delivery efficiency to distal airways that have undergone the loss of lung expansion and contraction capability.

II. METHODS

A. Geometry and mesh

Anatomical features of airway bifurcations are crucial because the branching pattern plays a major role in determining airflow and particle deposition. To reconstruct the airways tree following a similar SIP modeling strategy,[14,26] this study assumes that the airway branch follows the rules of regular dichotomy[48] after generation 3 (G3) to G17. Regular dichotomy means that each branch of a treelike structure gives rise to two daughter branches of identical dimensions. With such simplification, the truncated whole-lung modeling strategy[26–28] can be a feasible method to reduce the computational cost for the lung aerosol dynamics simulations from mouth/nose to alveoli without sacrificing computational accuracy.

Accordingly, the newly established elastic truncated whole-lung (TWL) model, which is a multi-path whole-lung model, consists of four sections: (1) mouth-to-throat (MT), (2) upper tracheobronchial (UTB) airways extending through G1 (second bifurcations), (3) five lower tracheobronchial (LTB) airways up to G16, representing the unsymmetrical 5-lobe human pulmonary routes, and (4) the heterogeneous acinus (see Figs. 1 and 2). Specifically, the first three sections represent the conductive airway zone extending from the mouth to the lowest bronchioles right before the start of the alveolar region. The MT and UTB geometries were created based on the realistic airway model of the human upper airway[4] constructed from the computerized tomography (CT) data of a healthy adult.[49] The LTB geometry was constructed using SolidWorks (Dassault Systèmes SolidWorks Corporation, Waltham, MA), with the symmetry assumption that the branching angles (ϕ_n) are the same in the bifurcations at the same generation. Figure 1 shows the schematic outline of the construction of the symmetric path model of the airway. The dimensions of the bronchi, i.e., airway radius (R_n), straight segment length (L_{t_n}), and branching angle (ϕ_n), are based on the data from ICRP.[51] The radius of the carinal ridge (r_n) is assumed to be equal to $0.5R_n$.[23] Each bifurcation was created in a different plane with an inclination angle (ψ_n), as indicated by the G_n plane and G_{n+1} plane as shown in Fig. 1. The range of ψ_n is from 30° to 65°,[51] and was determined by a series of random numbers generated in the same range. It is worth mentioning that the LTB geometry can be fully defined with parameters R_n, L_{t_n}, ϕ_n, r_n, and ψ_n. Table I lists all the parameters used for the LTB airway geometry generation.

The total branch length (L_n) is defined as the sum of three lengths [see Eq. (1)], i.e., the length of a segment contained in the daughter portion of the previous bifurcation (l_{a_n}), a straight length of the generation n (L_{t_n}), and the length of a segment contained in the parent portion of the successive bifurcation (l_{p_n})[23] (see Fig. 1). The total branch length L_n of the generation n (G_n) can be expressed as

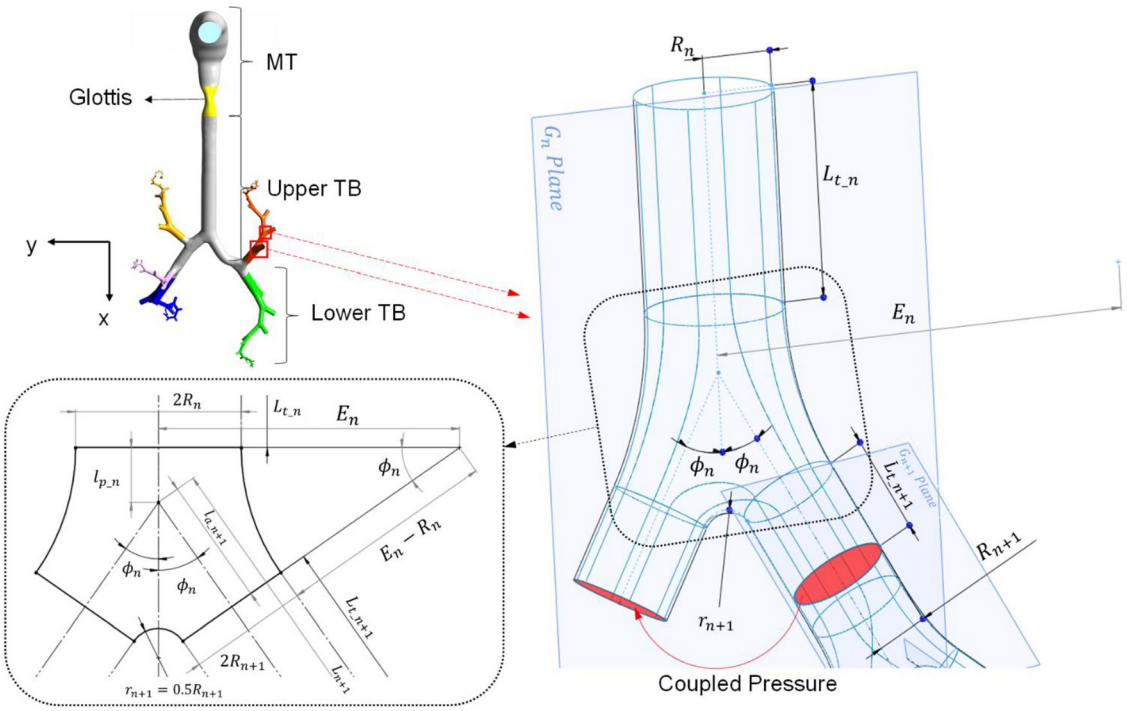

FIG. 1. Schematic diagram of the whole-lung airway geometry and construction of the truncated symmetric LTB geometry at G_n.

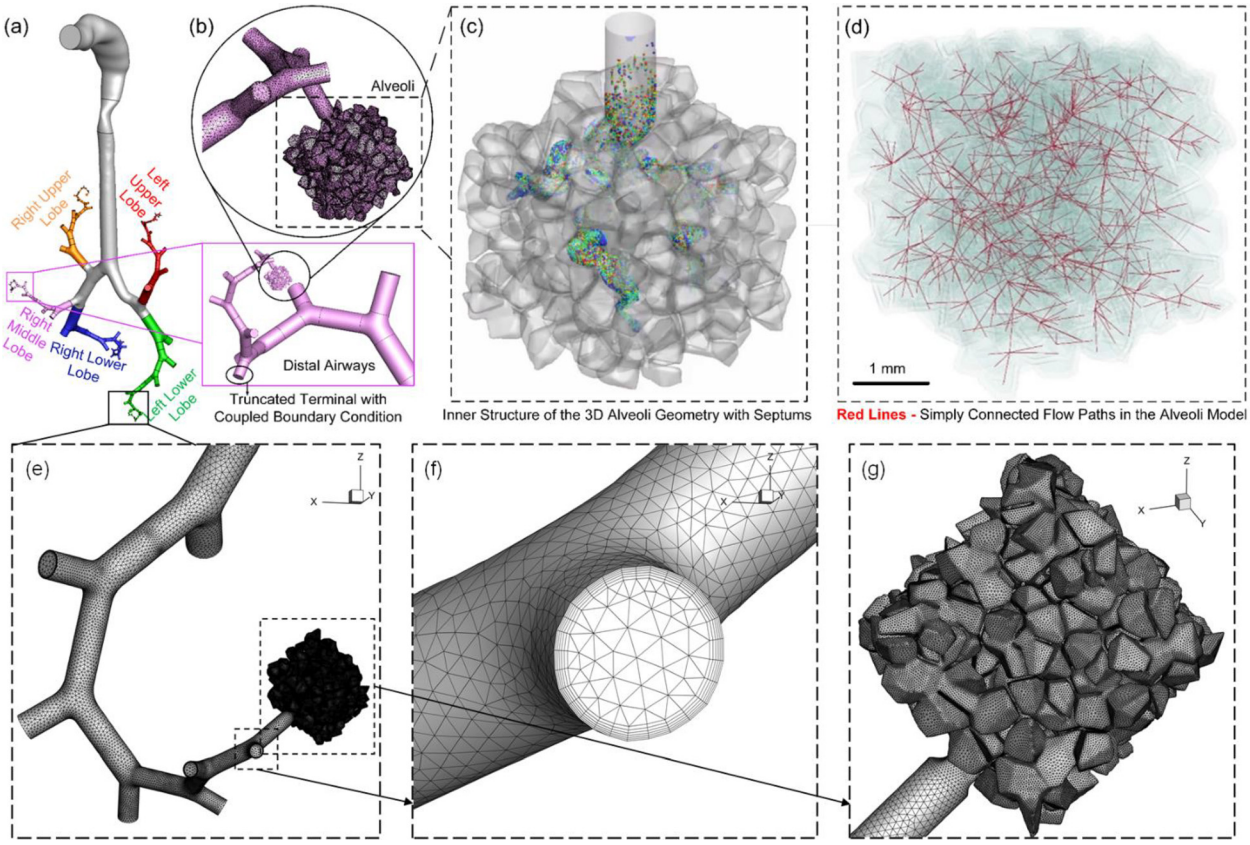

FIG. 2. Schematic diagram of the elastic TWL model with the reconstructed heterogeneous acinar model: (a) whole-lung geometry, (b) truncated small airway and alveoli structure, (c) acinus geometry, (d) airflow passages inside the acinus geometry, (e) small airway geometry and mesh (left lower lobe G11-alveoli), (f) enlarged airway outlet showing the hexahedral prism layers, and (g) alveoli structure with mesh.

$$L_n = l_{a\_n} + L_{t\_n} + l_{p\_n}, \tag{1}$$

where

$$l_{p\_n} = E_n \tan\phi_n - \frac{E_n/\cos\phi_n - (E_n - R_n + R_{n+1})}{\sin\phi_n}, \tag{2}$$

$$l_{a\_n} = \frac{E_{n-1}(1-\cos\phi_{n-1}) + (R_{n-1} - R_n)}{\sin\phi_{n-1}} \cos\phi_{n-1}. \tag{3}$$

Based on the symmetry assumption, the geometry of the LTB was reduced by truncating one of the daughter branches of each bifurcation in the model to reduce computational cost. The airflow pressure at the truncated plane is paired with the pressure of the cross-sectional plane at the corresponding location of the paring daughter branch.

The acinus model was created based on the algorithm developed by Koshiyama and Wada.[52] An illustration of the acinus structure and its dimensions are shown in Fig. 2. Specifically, the average volume of the five acini (one for each lobe) is 6.2×10^{-9} m^3, which is the residual volume (RV). The acinar geometry contains 406 alveoli with a mean generation of 6.7 (see Table II).

As shown in Fig. 2, The tetrahedral mesh with six near-wall hexahedral prism layers was generated using Ansys Fluent Meshing 2020 R2 (Ansys Inc., Canonsburg, PA). Mesh independence test was performed to find the mesh with the best balance between computational accuracy and time [see the supplementary online material (SOM) for more details]. The final mesh has 31 867 870 cells, and the minimum orthogonal quality is 0.12.

B. Generalized airway deformation function

The airway deformation kinematics in a full inhalation-exhalation breathing cycle is shown in Fig. 3, which includes the expansion-contraction motion of the TB tree and the glottis motion. In this study, dynamic mesh method was employed to describe the temporal and spatial nodal displacements of the computational domain, achieved using in-house C programs. The prescribed airway deformation can be defined mathematically. Specifically, the airway wall from trachea to G17 expands and contracts in all three directions [i.e., head-foot (x), arm-arm (y), and back-front (z) directions] with anisotropic deformation ratio x:y:z = 1:0.375:1[53,54] [see Fig. 3(a)].

TABLE I. Geometric characteristics of the human respiratory tract.[50]

Generation G_n	Airway radius R_n (mm)	Straight segment length L_{t_n} (mm)	Branching angle ϕ_n (°)	Radius of carinal ridge r_n (mm)	Inclination angle ψ_n (°)	E_n (mm)	l_{a_n} (mm)	l_{p_n} (mm)	Total branch length L_n (mm)
2	4.250	15.00	35	⋯	⋯	25.458	⋯	3.791	18.791
3	3.050	8.30	28	1.525	53	11.097	8.604	2.017	18.921
4	2.200	9.00	35	1.1	35.7	8.021	4.713	2.205	15.918
5	1.800	8.10	39	0.9	54.7	8.85	3.334	2.080	13.514
6	1.450	6.60	34	0.725	31.1	3.135	3.225	1.059	10.884
7	1.200	6.00	48	0.6	33.4	1.965	1.621	0.729	8.350
8	1.000	5.30	53	0.5	58.8	1.515	1.130	0.556	6.986
9	0.825	4.37	54	0.4125	41.1	1.464	0.899	0.505	5.774
10	0.675	3.62	51	0.3375	63.3	1.564	0.820	0.483	4.923
11	0.545	3.01	46	0.2725	31.2	1.19	0.789	0.374	4.173
12	0.440	2.50	47	0.22	45.4	1.183	0.615	0.486	3.602
13	0.410	2.07	48	0.205	43.4	0.545	0.554	0.126	2.750
14	0.300	1.70	52	0.15	31.6	0.875	0.352	0.313	2.365
15	0.265	1.38	45	0.1325	47.4	1.078	0.397	0.399	2.176
16	0.255	1.10	42	0.1275	32	0.576	0.425	0.236	1.761
17	0.230	0.92	50	0.115	⋯	⋯	⋯	⋯	⋯

The reduced deformation in y direction is due to the rib cage restriction. Furthermore, the glottis region opens and closes only in the y direction.[3] To define the above-mentioned airway deformation kinematics, a generalized function to prescribe the nodal displacements of the airway walls is given by

$$x_i^n = x_{i,r} + \frac{f_t(t^n)}{f_t(t^{n-1})} f_s\left(x_i^{n-1}\right)\left(x_i^{n-1} - x_{i,r}\right), \tag{4}$$

$$f_t(t^n) = 1 + \frac{d_{t,i}}{2}\left(1 - \cos\frac{2\pi t^n}{T_c}\right), \tag{5}$$

$$f_s\left(x_i^n\right) = \begin{cases} 0.5\left[1 - \cos\dfrac{(x_i^n - x_b)\pi t^{n-1}}{x_a - x_b}\right] & \text{for trachea } (i = 1) \\ 0.5\left[1 - \cos\dfrac{(x_i^n - x_a)\pi t^{n-1}}{x_b - x_a}\right] & \text{for trachea } (i = 2,\ 3) \\ 1 \quad \textit{for other regions} \end{cases}, \tag{6}$$

where $x_i = (x, y, z)$ is the coordinate of each node within the dynamic region (excluding glottis), $x_{i,r} = (x_r, y_r, z_r)$ is the reference point, t^n is the current time step, T_c is the time period of a full breathing cycle, and $d_{t,i}$ are the deformation ratios of airways. To achieve a smooth transition from the location where the expansion and contraction starts at the trachea to the first bifurcation, $f_s(x_i^n)$ was integrated into Eq. (4). $f_s(x_i^n)$ is defined by Eq. (6), in which x_a and x_b are the x-coordinates defining the upper and lower boundaries of the smooth transition region in trachea. For the TWL model used in this study, $x_a = 0.12$ m and $x_b = 0.18$ m, where the center of mouth opening locates at $x = 0$ (see Fig. 1).

TABLE II. Geometric details of the heterogeneous acinus model.

No. of alveoli	406
Min. generation	3
Max. generation	11
Mean generation	6.7

The glottis motion functions and corresponding numerical investigation results can be found in the previous publication.[3] Specifically, the glottis motion functions are expressed as

$$x_i^n = (d_{g,r} - 1) f_g\left(x_i^{n-1}\right) g(t^n) + x_{i,g}^0, \tag{7}$$

$$f_g\left(x_i^n\right) = \begin{cases} \sin^m\left(\dfrac{x_1^{n-1} - x_{g,a}}{x_{g,b} - x_{g,a}}\pi\right) & \textit{for } i = 2, \\ 0 \quad \textit{for } i = 1 \textit{ and } 3 \end{cases} \tag{8}$$

$$g(t^n) = a_0 + \sum_{\beta=1}^{n}\left[a_\beta \cos\left(\beta\omega t^{n-1}\right) + b_\beta \sin\left(\beta\omega t^{n-1}\right)\right], \tag{9}$$

where $x_{i,g}^0$ is the initial coordinates of the node in the moving glottis region, and $d_{g,r}$ is the deformation ratio of glottis between maximum glottis width and the width of the glottis at the neutral position as shown in Fig. 3(b). Similarly, $x_{g,a} = 0.056$ m and $x_{g,b} = 0.076$ m are the x coordinates that define the boundaries of smooth transition in the glottis region. In addition, the nodal displacement function $g(t^n)$ is a time-dependent Fourier series that controls the nodal motion separately. It is worth mentioning that $g(t^n)$ is simplified as a single-term sinusoidal function, which is employed to simulate the idealized glottis motion in this study [see Fig. 3(b)].

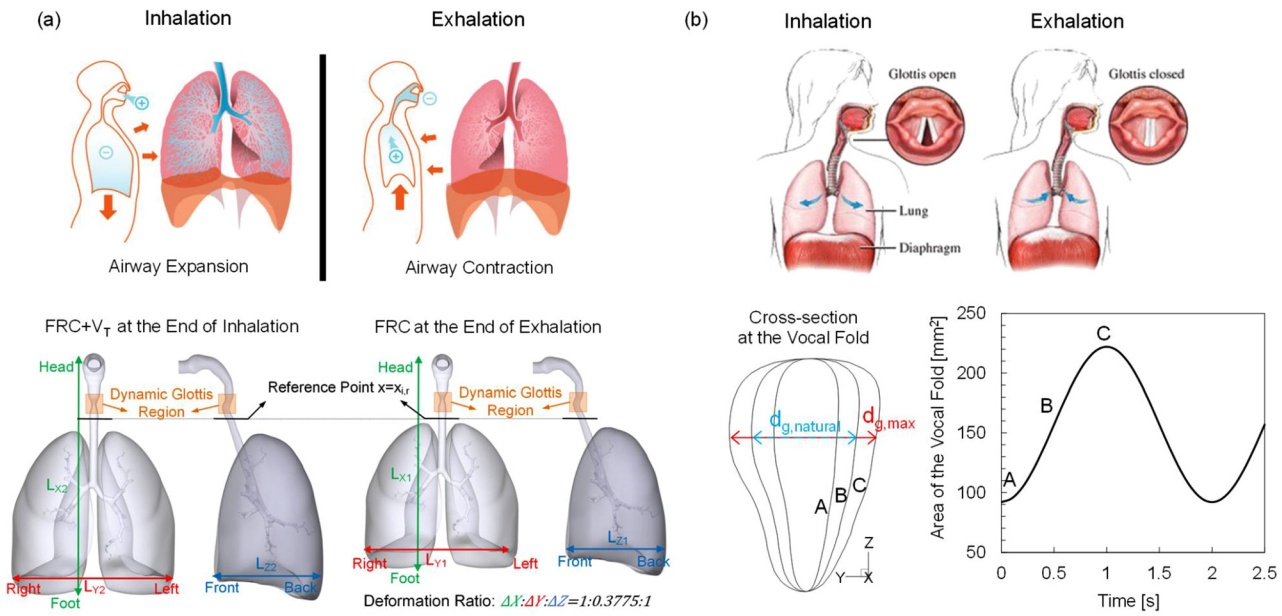

FIG. 3. The deformation kinematics of (a) the TB tree (the top images were reproduced from https://courses.lumenlearning.com/boundless-biology/chapter/breathing/) and (b) glottis in a full inhalation-exhalation cycle[69,70] (the top images were reproduced from https://www.vocalclinic.org/theprocessofspeakingandsinging.htm).

By adjusting the values of $d_{t,i}$, the TWL model can simulate disease-specific airway deformation kinematics representing a healthy lung and lungs with multiple COPD conditions. The values of $d_{t,i}$ and the corresponding lung conditions are listed in Table III. The calibration and validation of the airway deformation kinematics can be found in Sec. III A.

C. Computational fluid-particle dynamics (CFPD) model

CFPD models, especially the one-way coupled Euler–Lagrange models, have been widely employed for modeling the airflow and micro/nano particle transport and deposition in human respiratory systems. The one-way coupled Euler–Lagrange based model employed in this study used Ansys Fluent 2020 R2 (Ansys Inc., Canonsburg, PA) enhanced with in-house user-defined functions (UDFs) in C/C++ to predict the particle dynamics in the laminar-to-turbulence flow fields inside the airways.

1. Continuous phase: pulmonary airflow

In this study, airflow is assumed to be isothermal and incompressible ($\rho = 1.204\,\text{kg/m}^3$), with a dynamic viscosity $\mu = 1.825 \times 10^{-5}$ Pa·s. The continuity and Navier–Stokes (N–S) equations with moving boundaries can be given by

TABLE III. Deformation ratio of airways for different lung conditions.

$d_{t,i}$	0.4	0.36	0.2
Lung condition	Healthy	Mild COPD	Severe COPD

$$\frac{\partial(u_i - u_i^{mov})}{\partial x_i} = 0, \tag{10}$$

$$\frac{\partial u_i}{\partial t} + (u_j - u_j^{mov})\frac{\partial u_i}{\partial x_j} = -\frac{1}{\rho}\frac{\partial p}{\partial x_i} + \frac{\mu}{\rho}\frac{\partial \tau_{ij}}{\partial x_j} + g_i, \tag{11}$$

$$\tau_{ij} = \mu\left[\left(\frac{\partial u_i}{\partial x_j} + \frac{\partial u_j}{\partial x_i}\right) - \frac{2}{3}\mu\delta_{ij}\frac{\partial u_k}{\partial x_k}\right]. \tag{12}$$

The convective velocity $u_i - u_i^{mov}$ in Eq. (11) is induced by the difference between the air velocity u_i and the dynamic mesh velocity u_i^{mov} describing the airway deformation. u_i^{mov} can be given by

$$u_i^{mov} = \partial x_i/\partial t, \tag{13}$$

where x_i for the region from the trachea to alveoli (i.e., $x_1 > 0.12$ m) can be obtained from Eq. (4), and x_i of the moving glottis region (i.e., $0.056\,\text{m} < x_1 < 0.076$ m) can be obtained from Eq. (7). The transitional characteristics of the pulmonary airflow are modeled using k-ω Shear Stress Transport (SST) model, which has been extensively validated in previous works.[4,55,56]

2. Discrete phase: inhaled particle transport dynamics

The one-way coupled Euler–Lagrange approach has been widely used and experimentally validated for pulmonary particle-laden airflow predictions.[4,8,57] The governing equations for discrete particle phase has been provided in previous publications.[4,8,57] Particles are assumed to be spheres with constant aerodynamic diameter. In this study, particles with different diameters, i.e., $d_p = 0.1$, 0.2, 0.5, 1.0, 2.0, 5.0, and 10.0 μm, are investigated. The velocity and trajectory of every single particle are calculated by solving Newton's second law, which considers the drag force, gravitational force, random force induced by

Brownian motion, and the force induced by turbulence dispersion.[3,4] Furthermore, the regional deposition of particles in the airways can be calculated by regional deposition fraction (DF), i.e.,

$$DF_{\text{specific region}} = \frac{\text{Mass of particles deposited in a specific region}}{\text{Mass of particles injected through the mouth opening}}. \quad (14)$$

3. Boundary and initial conditions

The starting time and initial conditions of the airway model are at the end of a previous inhalation–exhalation cycle, which mimics the inhalation of aerosolized drug particles in real-world inhalation therapy scenarios. At the end of exhalation, the lung capacity is equal to the residual volume defined in the pulmonary function test (PFT). The pressure of the truncated branch outlet is coupled with the pressure of the identical surface at its paired daughter branch (see Fig. 1). A full breathing cycle of 2 s is simulated, including both inhalation and exhalation. The breathing profile at the mouth is determined only by the lung deformation kinematics. Accordingly, for the elastic lung model, the pressure-inlet boundary condition is specified at the mouth opening, where atmosphere pressure is assumed. A total of 50 000 particles are released at the mouth from time $t = 0.2$ to 0.25 s, which is aligned with the duration of drug particle emissions from inhalers.[58] Specifically, 10 000 particles are injected per 0.001 s. The initial velocity of particle is set to 0 as the particles can be accelerated to the flow velocity within the extending section at the mouth opening [see Fig. 2(a)]. Particles are considered "deposited," when the distance between the center of the particle and the airway wall is less than the particle radius.

D. Numerical setup

The numerical approach, i.e., the elastic TWL model used in this study, is based on the in-house prescribed dynamic mesh method, one-way coupled Euler–Lagrange method,[3] and k-ω Shear Stress Transport (SST) model, which enables the predictions of anisotropic airway deformation and air-particle flows in the whole-lung in tandem where turbulent, transitional, and laminar flows coexist. To realize the algorithm mentioned above, in-house UDFs were developed and compiled for the following:

(1) specifying the airway deformation kinematics;
(2) specifying the coupled pressure boundary conditions at truncated branch outlets;
(3) recovering the anisotropic corrections on turbulence fluctuation velocities;
(4) modeling the Brownian motion induced forces;
(5) storing particle deposition data.

The CFPD simulations were executed using Ansys Fluent 2020 R2 (Ansys Inc., Canonsburg, PA) and performed on a local Dell Precision T7910 workstation (Intel® Xeon® Processor E5–2683 v4 with dual processors, 32 cores, and 256 GB RAM), the supercomputer "Pete" at the High Performance Computing Center (HPCC) at Oklahoma State University (OSU) (Intel® Xeon® Processor Gold 6130 CPU with dual processors, 32 cores, 64 threads, and 96 GB RAM), and Microsoft Azure (120 AMD EPYC 7V12 processor cores with 4 GB RAM per CPU core) enabled by Ansys Cloud Computing COVID-19 HPC Consortium. The Semi-Implicit method for pressure-linked equations (SIMPLE) algorithm was employed for the pressure-velocity coupling, and the least squares cell-based scheme was applied to calculate the cell gradient. The second-order scheme was employed for pressure discretization. In addition, the second-order upwind scheme was applied for the discretization of momentum and turbulent kinetic energy. Convergence is defined for continuity, momentum, and supplementary equations when residuals are lower than 1.0×10^{-5}. Depending on the particle size simulated and the lung conditions, the computational time for completing one elastic TWL case on OSU HPCC ranges between 118 and 152 h. The computational time for completing one static TWL case on OSU HPCC ranges between 22 and 42 h.

III. MODEL CALIBRATION AND VALIDATION

A. Validation and calibration of the elastic TWL model

The elastic TWL model was first validated by comparing the total lung volume change during a full breathing cycle predicted by the numerical method with experimentally measured results from the literature[47,59,60] (see Fig. 4). It should be noted that the initial lung volume equals residual volume (RV) (see Fig. 5 for the definition of RV). Moreover, to calculate the whole lung volume of the elastic TWL model, the acinus volume is multiplied by 2^{15} (i.e., 15 generations were truncated) to recover the total volume of a whole lung. The total lung volume through breathing matches well with the data in the open literature. Thus, the generalized airway deformation function and the elastic TWL model [see Eqs. (4)–(6)] have been proved to be able to capture the deformation kinematics of a real human respiratory system.

To model the disease-specific airway deformation kinematics, the elastic TWL model was calibrated by varying the values of $d_{t,i}$ [see Eq. (5)]. Specifically, the values of $d_{t,i}$ are determined by matching the total lung capacity (TLC) under two COPD conditions, i.e., mild and severe COPD, as well as the TLC of a healthy lung. It should be noted that lung RVs are assumed to be the same for healthy and diseased lungs. Lung volumes under different health conditions, including one normal healthy condition and three COPD conditions[61] are given in Fig. 5(a). Correspondingly, the lung volume changes calculated using the elastic TWL model are given in Fig. 5(b). It is evident that the numerically

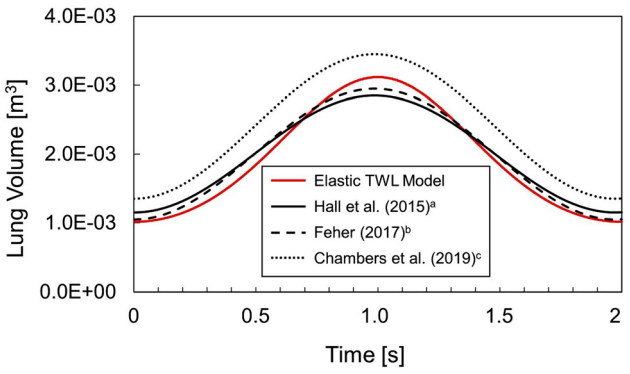

FIG. 4. Validation of the elastic TWL model: comparison of the total lung volume of the elastic TWL model and experimentally measured data.[47,59,60]

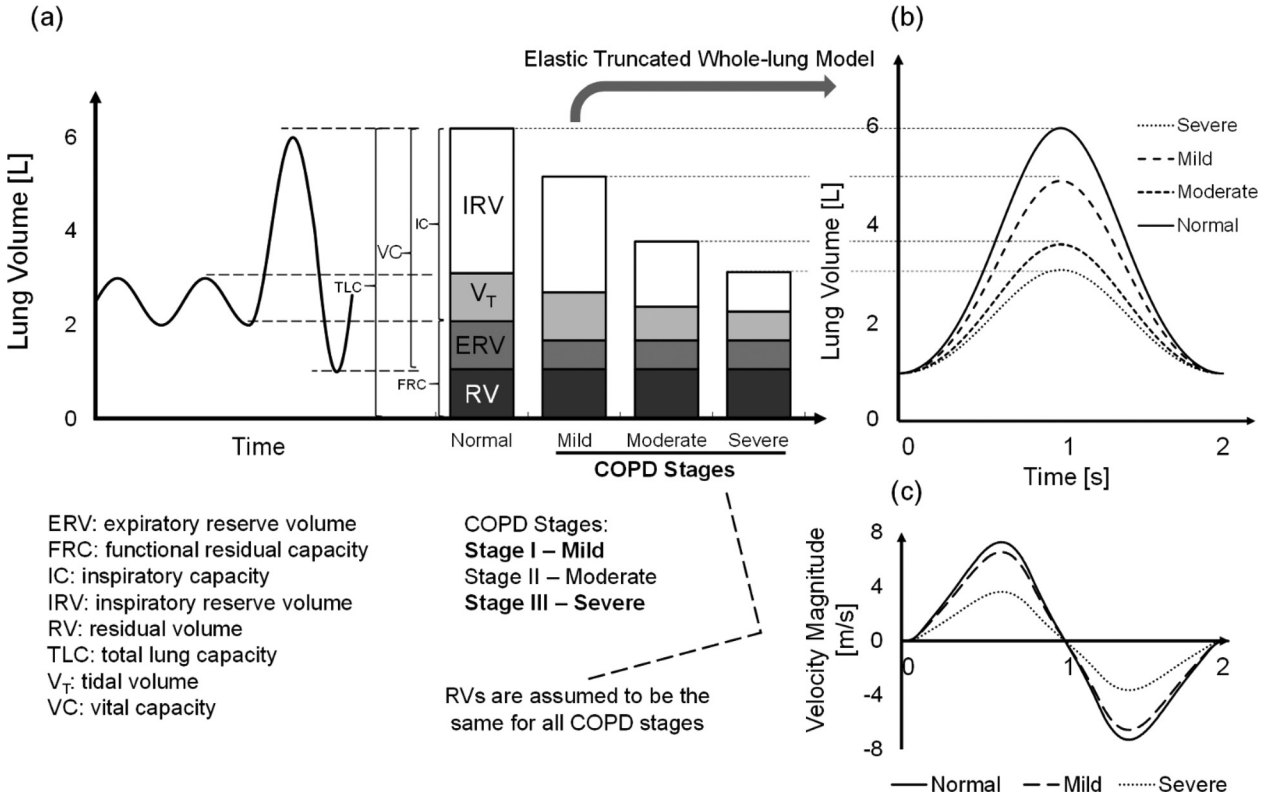

FIG. 5. Calibrations of the lung volume change predictions using the elastic TWL model via matching pulmonary function test (PFT) data[61] for different lung disease conditions: (a) PFT data of lung volume changes under different health conditions, including one healthy condition and three COPD stages,[61] (b) lung volume changes predicted using the elastic TWL model, and (c) the breathing profile at the mouth opening induced by the lung volume change.

predicted TLC under different lung conditions matches very well with the clinical data from the literature.[61] The value of $d_{t,i}$ for different lung conditions is given in Table III.

B. CFPD model validation

The k-ω SST model has been extensively validated and employed in previous research to resolve the flow field based on its ability to predict pressure drop, velocity profiles accurately, and shear stress for both transitional and turbulent flows.[4,55,56] Specifically, the representative Reynolds number (Re) and turbulence kinetic energy (TKE) at the peak of inhalation (t = 0.5 s) in multiple generations in this study are listed in Table IV. It can be observed that at the peak inhalation, the airflow is turbulence from mouth to G5, and the flow relaminarization happens after G5. Therefore, during the full inhalation-exhalation cycle, the airflow is mainly laminar-to-turbulence transitional flow in the mouth-to-G5 region, and laminar in the G5-to-alveoli region. The one-way coupled Euler–Lagrange method was also well-proved with *in vitro* and *in vivo* data in the previous research for accurate predictions of the aerosol dynamics in human respiratory systems.[4,16,62,63]

In this study, the particle deposition fraction (DF) predicted using the static TWL model at a steady inhalation flow rate of 30 l/min was compared with both numerically predicted and experimentally measured data from open literature.[16,64] Table V compares the total DF of particles with d_p = 1.0, 2.0, and 5.0 μm. In general, the total DF either predicted by numerical methods or measured experimentally follows the same trend as d_p increases from 1.0 to 5.0 μm. It can be noticed that the static TWL model predicts slightly lower total DF for all three sizes of particles tested compared with literature data. This

TABLE IV. Typical Reynolds numbers (Re) and turbulence kinetic energy (TKE) at different locations of the airway at the peak inhalation (t = 0.5 s).

	Normal		Severe	
	Re	TKE	Re	TKE
Oral cavity	6.68×10^3	2.16×10^{-1}	4.51×10^3	8.72×10^{-2}
Vocal folds	1.44×10^4	1.78×10	9.90×10^3	7.82×10^1
G0	1.07×10^4	1.65×10	7.32×10^3	8.44×10^1
G2	4.95×10^3	2.32×10	3.40×10^3	1.15×10
G3	3.74×10^3	1.29×10	2.49×10^3	5.46×10^{-1}
G5	1.31×10^3	4.49×10^{-1}	8.34×10^2	1.50×10^{-1}
G6	8.97×10^2	3.11×10^{-1}	5.86×10^2	1.02×10^{-1}
G7	5.78×10^2	2.05×10^{-1}	3.81×10^2	5.20×10^{-2}
G17	3.53×10^3	1.0×10^{-14}	1.43×10	1.0×10^{-14}

TABLE V. Total lung deposition fraction (DF) comparison with benchmark deposition data in open literature.[16,64]

d_p (μm)	Static TWL	Longest *et al.*[16]	Stahlhofen *et al.*[64]
1.0	17.5%	32.8%	24.2%
2.0	38.4%	44.2%	45.3%.
5.0	71.5%	75.4%	81.0%

difference in total DF could be related to the different airway structures used in the three studies.

IV. RESULTS AND DISCUSSION

A. Airflow characteristics: static TWL vs elastic TWL

The pulmonary airflow features (i.e., laminar-to-turbulence transition and relaminarization) are investigated. Specifically, the representative Reynolds number (Re) and turbulence kinetic energy (TKE) at peak inhalation at different generations in the whole-lung model are listed in Table IV. It can be noted that at peak inhalation (t = 0.5 s), the airflow in the upper airway (above G5) is mainly turbulence although the TKE in the oral cavity is low. The flow fluctuation increases in the glottis regions with the laryngeal jet extended into G3. It can be observed from Table IV that TKE increases from G0 to G2, which can be due to the reduced hydraulic diameter. After airflow passes G5, relaminarization starts. Re decreases gradually from G5 to alveoli. Re is less than 2 at G17. In addition, healthy lung deformation kinematics resulted in higher Re and TKE than severe COPD lung at all monitoring locations selected from mouth to alveoli.

To evaluate the significance of airway deformation on pulmonary airflow characteristics and determine the necessity to employ the elastic TWL model, the pulmonary airflow fields predicted by static TWL and elastic TWL models are compared. The widely used static lung modeling framework has two major differences compared with the elastic TWL model:

(1) The static lung modeling framework uses velocity mouth/nose inlet condition instead of realistic pressure boundary conditions due to the absence of the acinus structure in the static lung model.
(2) The static lung modeling framework neglects glottis and TB tree deformation kinematics.

To compare the airflow fields, one full breathing cycle was simulated for three lung conditions, i.e., normal, mild COPD, and severe COPD, using the elastic TWL model. The static TWL model was also employed to predict the airflow structure for those three lung conditions, with sinusoidal breathing mass flow rate waveforms applied at the mouth opening. The sinusoidal waveform functions providing the equivalent lung volume changes, which were obtained from the elastic TWL simulation results to minimize the influence of potential boundary condition differences between static and elastic TWL models. The comparisons of inspiratory airflow structures at the sagittal plane are given in Figs. 6 and 7. The normalized velocity $\tilde{\vec{V}}$ is nondimensionalized using the averaged velocity at mouth opening at the peak

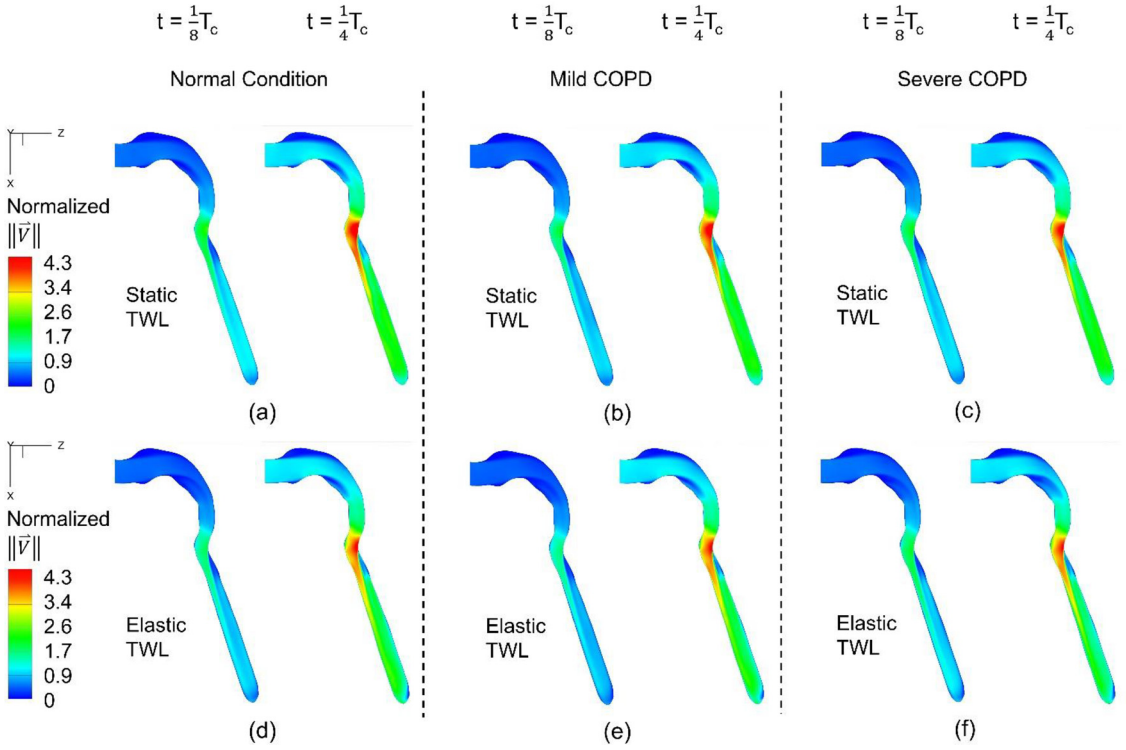

FIG. 6. Normalized velocity magnitude contour at the sagittal plane (y = 0): (a) static model with normal healthy condition, (b) static model with mild COPD, (c) static model with severe COPD, (d) elastic model with the normal healthy condition, (e) elastic model with mild COPD condition, and (f) elastic model with severe COPD condition.

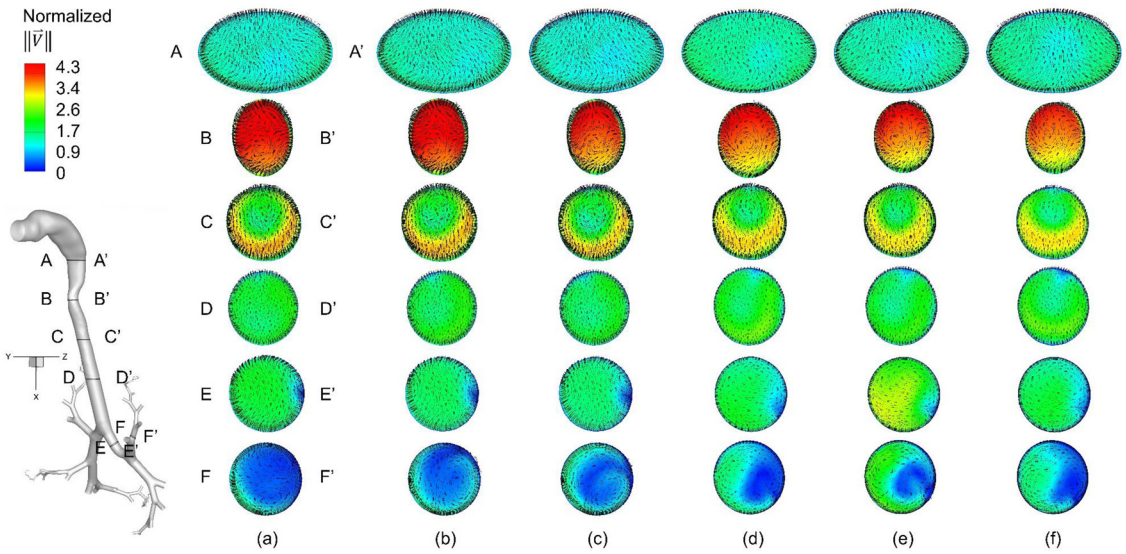

FIG. 7. Normalized velocity magnitude contour and tangential velocity vector on selected slices at $t=\frac{1}{4}T_c$ for cases: (a) static model with normal healthy condition, (b) static model with mild COPD, (c) static model with severe COPD, (d) elastic model with normal healthy condition, (e) elastic model with mild COPD, and (f) elastic model with severe COPD.

inhalation flow rate ($t = \frac{1}{4}T_c$). Since the inhaled particle transport and deposition are dominantly influenced by the inspiratory airflow, Fig. 6 shows the normalized velocity contour at the sagittal plane ($y = 0$) at $t = \frac{1}{8}T_c$ and $t = \frac{1}{4}T_c$. It can be observed that the airflow pattern during inhalation changes significantly as the flow rate reaches its peak value. The mouth jet and laryngeal jet become much stronger at $t = \frac{1}{4}T_c$ than $t = \frac{1}{8}T_c$. All six cases show a similar inspiratory airflow structure, except that the elastic TWL model predicts relatively weaker laryngeal jets extended from the glottis than the static TWL model for all three lung conditions. Such differences are mainly due to the wider glottis openings in elastic TWL simulations than the static TWL simulations. In addition, the elastic TWL model predicts weaker convection in the oropharynx for severe COPD conditions [see Fig. 6(f)] compared with normal and mild COPD conditions [see Figs. 6(d) and 6(e)], which is due to the decreases in TB tree expansion amplitude with the increase in the COPD severity (see Fig. 5).

To further visualize the lung deformation effect on airflow patterns in MT, trachea, and G1-to-G3 regions, $\sim \vec{V}$ contours and tangential velocity vector distributions on selected cross sections (i.e., AA′ to EE′) at the peak inhalation flow rate ($t = \frac{1}{4}T_c$) are given in Fig. 7. Specifically, the flow structures shown in AA′ are similar for all six cases, with no evident differences in secondary flows. This indicates that during the inhalation, the glottis motion and TB expansion have minor effect on the airflow patterns in the oropharynx since viscous dissipation effect on the airflow patterns. At BB′ where is the glottis, one can notice the glottis expansion in elastic TWL model cases [see Figs. 7(d)–7(f)]. As a result of the glottis expansion, differences in airflow patterns can be observed at BB' between static and elastic TWL simulation results. For normal conditions [see Figs. 7(a) and 7(d)], although both static and elastic TWL simulations predict counterclockwise in-plane recirculation near the center of BB′, the vortices locate more to the left in the elastic TWL simulation than the static TWL simulation. Also, the secondary flow has different directions on the top left corner of BB′. In addition, $\vec{V}$ at CC′ and DD′ shows the skewed velocity distributions induced by the laryngeal jets in the trachea. It can be seen from CC′ that two counter-rotating vortices are formed at the center of CC′ in the static TWL model, while only one counterclockwise vortex can be observed in the elastic TWL model. The reason for such differences is determined by whether the glottis and trachea expansion are included or neglected in the TWL model. Explicitly, the vocal fold and trachea expand during inhalation [see Fig. 3(b)]. Thus, compared with the elastic TWL model, the static TWL case predicts higher flow velocity at the throat-to-trachea region and higher intensity of laryngeal jet impact, hence possibly higher shear velocity, which leads to two vortices at CC′. In contrast, only one counterclockwise vortex is preserved at CC′ in the elastic TWL case due to the larger cross-sectional area induced weaker secondary flow intensities. Moreover, $\vec{V}$ contour at CC′ shows that the static TWL model predicts higher $\vec{V}$ at the anterior of the trachea (i.e., bottom of CC′) for normal and mild COPD conditions than the other cases. In slice DD′, the counterclockwise secondary flow existing upstream is diminished and challenging to be observed. As the flow enters the first bifurcation (i.e., EE′), airflow structures between static and elastic TWL models are highly different. For the static TWL model, vortices can be found on both left and right sides in EE′. However, in the elastic TWL model, the vortices shift to the top-right and bottom left of slice EE′. After the third bifurcation (i.e., FF′), the airflow structure is affected by lung deformation kinematics and the inhalation flow rate (lung conditions). Specifically, at FF′, although Dean's flows can be observed in all cases, the predicted location and number of the vortices differ between static and elastic TWL models. Thus, it can be concluded that the neglected airway deformation kinematics has a minor influence on the inspiratory airflow fields from mouth to AA′. In contrast, the effect of lung deformation kinematics on airflow structure becomes manifest from BB′ to FF′, which represents the glottis to G3.

Furthermore, it can also be concluded that the lung disease condition induced difference in airway deformation kinematics can lead to different pulmonary airflow patterns from the glottis to G3 and possibly further downstream. This indicates the necessity to model airway motions on a disease-specific level.

B. Effect of airway deformation kinematics on particle transport and deposition patterns

To further investigate how the neglected airway deformation kinematics can influence the predictions of lung aerosol dynamics, the transport and deposition of particles with different diameters (i.e., $d_p = 0.1$, 0.2, 0.5, 1.0, 2.0, 5.0, and 10.0 μm) in the TWL model are investigated individually under the above-mentioned three lung conditions (see Table III). As an example, deposition distributions of particles with $d_p = 0.1$, 1.0, and 10.0 μm in both the static and elastic TWL models after one full inhalation-exhalation breathing cycle are visualized in Figs. 8(a)–8(f). For all the cases shown in Figs. 8(a)–8(f), concentrated particle depositions occur in the throat, the main bronchus, and the first three bifurcations. However, the differences in particle deposition distributions predicted by static and elastic TWL models are significant. Specifically, at the normal lung condition [see Figs. 8(a) and 8(d)], particles are more likely to be entrapped in the trachea of the static TWL model compared with the elastic TWL model. Previous research demonstrates that Brownian motion induced force has a strong impact on the transport and deposition of small particles ($d_p < 0.5\,\mu$m), while the inertia impaction on small particle depositions (e.g., $d_p < 0.5\,\mu$m) is negligible. This explains the deposition of 0.1-μm particles in the trachea for the static TWL model. In contrast, with the trachea expansion during the inhalation, 0.1-μm particles had less chance to touch the airway wall in elastic TWL simulations compared with the static TWL simulations. Additionally, the static TWL model also predicted a significantly higher deposition in the trachea for 1.0 μm particles than the elastic TWL model [see Figs. 8(a) and 8(d)]. The deposition differences in the trachea between static and elastic TWL models are also partially due to the different intensities of the secondary flow observed in Fig. 7(a) at BB′ and CC′. Specifically, in the elastic TWL model, the wider glottis opening during inhalation induced weaker laryngeal jet impaction in the trachea, which creates the difference in airflow patterns in the trachea and contribute to the deposition differences between the static and elastic TWL models. For the deposition distributions of 10-μm particles shown in Figs. 8(a) and 8(d), another interesting observation is the "delayed" particle deposition in elastic TWL simulations than static TWL simulations. Specifically, although a lower deposition concentration of 10.0 μm particles in the trachea is observed in the elastic TWL model than the static TWL model, the deposition concentration is higher in the first two bifurcations of right lobes in the elastic TWL model. This is due to the fact that the TB airway wall expansion reduces the chances for particles to touch the airway wall and delays the deposition of particles more to the downstream airways. The static TWL model predicts much higher deposition concentration in MT of large particles ($d_p = 10\,\mu$m) than elastic TWL model. This observation agrees with the findings of the authors' previous research on the effect of glottis motion on particle transport and deposition in an upper airway model.[3] Similar comparisons between elastic and static TWL

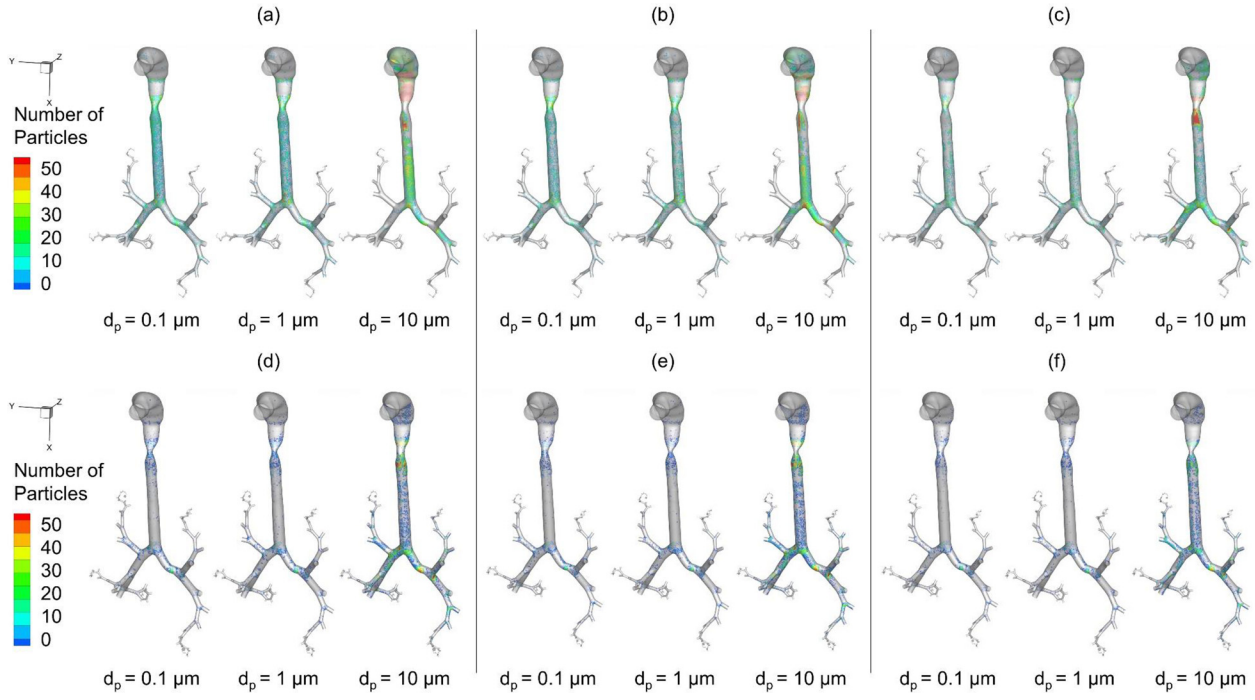

FIG. 8. Lung deposition distributions of particles with multiple diameters (dp = 0.1, 1.0, and 10 μm): (a) static model with the normal healthy condition, (b) static model with mild COPD, (c) static model with severe COPD, (d) elastic model with the normal healthy condition, (e) elastic model with mild COPD, and (f) elastic model with severe COPD.

simulation results can be observed for mild and severe COPD conditions shown in Figs. 8(b), 8(c), 8(e), and 8(f). The effects of disease conditions on inhaled particle transport and deposition are further discussed in Secs. IV C–IV E.

C. Effect of airway deformation and disease conditions on total DFs

The effect of lung deformation on particle deposition is also analyzed by comparing the total deposition fractions (DFs) of particles with d_p ranging from 0.1 to 10 μm under different lung health conditions (see Fig. 9). In general, it can be observed from Fig. 9 that both static and elastic TWL models are able to predict the classic "U-curve" total DF as a function of d_p. This is demonstrated extensively in previous research.[4,16] For lungs under normal condition, the static TWL model predicts 13.4% higher total DF of particles with $d_p = 0.1$ μm than the elastic TWL model. For particle size ranging from 0.2 to 2.0 μm, the total DF differences predicted by the static and elastic TWL models are relatively small which are approximately 7%. However, as particle size increases to 5.0 and 10.0 μm, the static TWL model predicts 16.9% and 13.1% less total DFs than the elastic model, respectively. For the mild COPD condition, the difference in total DF predicted by static and elastic TWL models is not obvious. Specifically, the highest difference is 5.1% as the elastic TWL model generates a higher total DF for particles with $d_p = 0.2$ μm than the static model. For the severe COPD condition, both static and elastic TWL models predict similar total DF for small ($d_p = 0.1$ and 0.2 μm) and large ($d_p = 10$ μm) particles. However, for particles with d_p between 0.5 and 5 μm, the static TWL model gives lower total DFs than the elastic TWL model. Especially for $d_p = 2$ μm, the static model predicts 16% lower total DF than the elastic model. It can be concluded that a static TWL model can be used instead of the more physiologically realistic elastic TWL model for predicting the total DF of particles ($0.1 < d_p < 10$ μm) for airways under mild COPD condition only. For other lung health conditions, the more physiologically realistic TWL model should be employed to more accurately reflect the airway deformation effect on particle transport and deposition.

D. Effect of airway deformation kinematics on regional DFs

To better understand the effect of airway deformation kinematics on particle dynamics in the respiratory system, regional DFs predicted by static and elastic TWL models are visualized and compared [see Figs. 10(a)–10(g)]. Explicitly, for particles with $0.1\ \mu\text{m} \le d_p \le 5\ \mu\text{m}$ [see Figs. 10(a)–10(f)], regardless of the lung conditions (i.e., normal, mild or severe), static TWL model predicts higher regional DFs in the TB tree (from MT to G7) while it predicts lower regional DFs in lower airways (G8 to acinus) than the elastic TWL model. The higher regional DF predictions using the static TWL model are due to the neglected airway expansions during the inhalation. As discussed in Sec. IV B, the expansions of glottis opening and the TB tree in the elastic TWL model can reduce the chance for particles to touch the airway wall, with the reduced intensity of the laryngeal jet impact in the trachea, thereby reducing the deposition due to the direct impaction and the afterward splash induced dispersion, especially for small particles ($d_p = 0.1$ μm). However, with the static airway, the Brownian motion effect increases the deposition possibility for small particles. This also explains the overprediction of the static TWL model on total DF of particles with $d_p = 0.1$ μm (see Fig. 9). In contrast, the lower regional DF predictions from G8 to acinus using the static TWL model can be also due to the reduced particle interceptions in small airways resulted from the reduced secondary airflow intensities because of the negligence of the airway deformation. Specifically, interception is the dominant mechanism for particle depositions in small airways. Physiologically realistic airway deformations can enhance the localized secondary flows, thereby increasing the particle interceptions with the airway wall in the elastic TWL simulations than static TWL simulations.

For particles with $d_p = 10$ μm, inertial impaction and gravitational sedimentations dominate their transport and deposition in the airways.[4,16] Similar to smaller particles, the simulation results show that the static TWL model predicts higher regional DFs of 10-μm particles in the upper airway (i.e., MT and glottis) than the elastic TWL model [see Fig. 10(g)]. Especially in MT, the static TWL case for healthy lung condition predicts $\text{DF}_{\text{MT}} = 47.8\%$ in contrast to $\text{DF}_{\text{MT}} = 1.8\%$ predicted by the elastic TWL case. The difference indicates that the effects of the reduced secondary flow and laryngeal jet impact induced by the glottis expansion decrease 10-μm particles deposition in MT and glottis. Furthermore, the regional DFs in UTB and lower airways predicted by the static TWL model is much lower than the elastic TWL model. For the static TWL model, most 10-μm particles deposited due to inertial impaction before reaching the main bronchi, and the rest particles either suspended in the airway or exhaled. For the elastic TWL model, as 10-μm particles enter the G1–G7 and G8-to–acinus regions, both inertial impaction and airway deformation induced secondary flow increase the chance of particle interceptions with the airways, which leads to higher DF in the G1–G7 and G8-to-acinus regions compared with the static TWL model. In addition, the static model predicts no deposition of large particles ($d_p = 10$ μm) after G8, while the elastic model shows that the DF of that particles is about 18.6% for a normal lung condition. In conclusion, static model overpredicts the DF in upper airways (from MT to UTB) and G1 to G7 and underpredicts the DF in lower airways (G8-acinus) for particles with $0.1\ \mu\text{m} \le d_p \le 5\ \mu\text{m}$ than elastic TWL models. For large particles ($d_p = 10$ μm), the only difference is that static model also underpredicts the DF in G1–G7. Therefore, to accurately evaluate the targeted delivery efficiency of inhaled drug particles, airway deformation kinematics should be considered in the simulations.

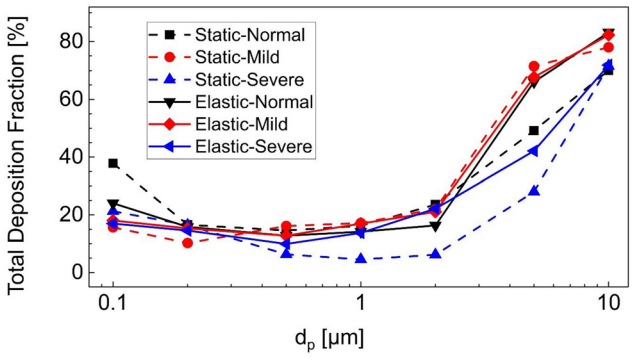

FIG. 9. Total deposition fractions (DFs) of particles in whole lung with diameters ranging from 0.1 to 10 μm under different lung health conditions.

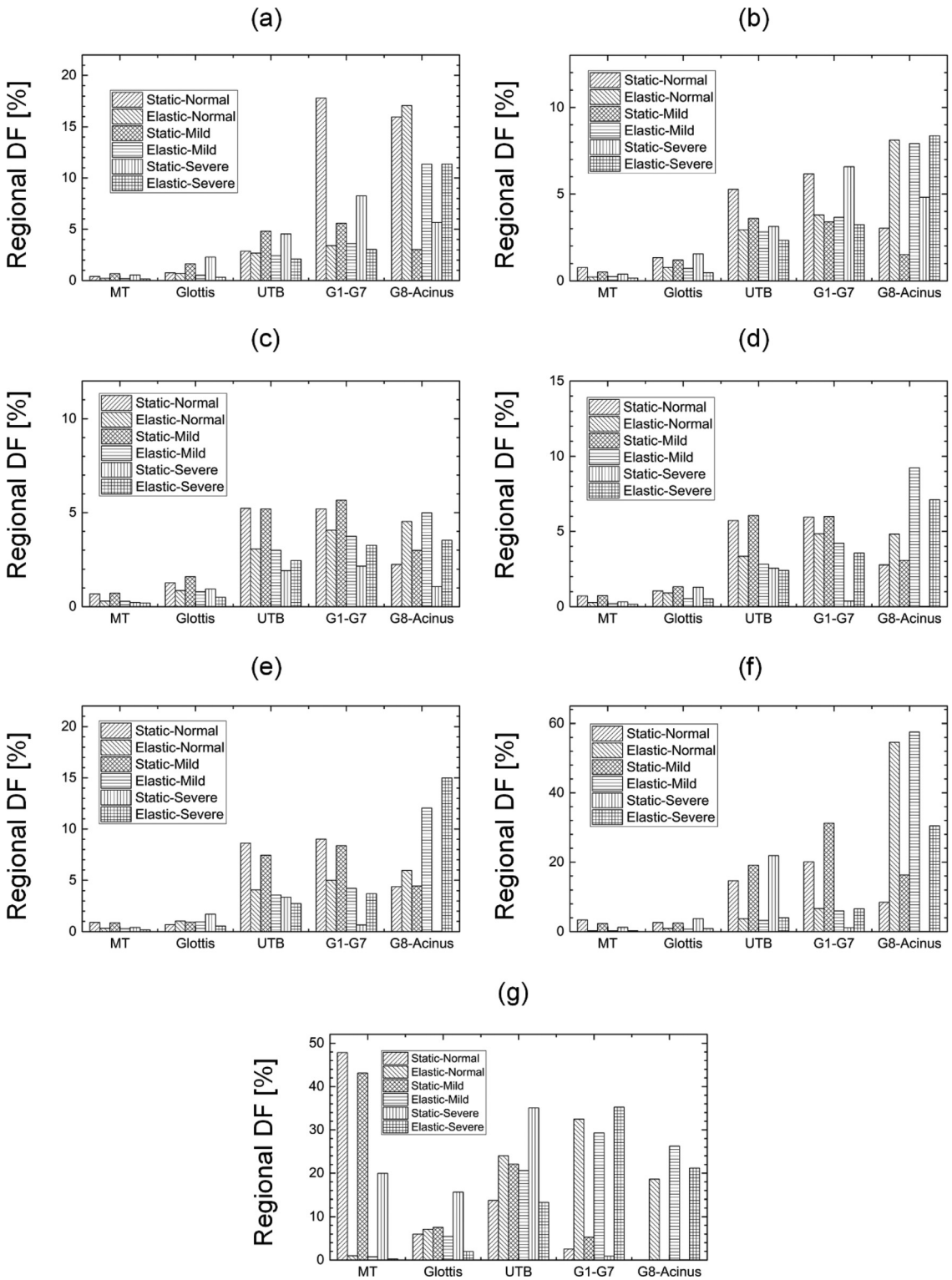

FIG. 10. Comparisons of regional DF predictions via static TWL model and elastic TWL model under three lung health conditions for particles with different diameters: (a) $d_p = 0.1$, (b) $d_p = 0.2$ (c) $d_p = 0.5$, (d) $d_p = 1.0$, (e) $d_p = 2.0$, (f) $d_p = 5.0$, and (g) $d_p = 10\ \mu$m.

With the insight into regional DF, it is possible to explain the differences in total DF predicted by static and elastic models for different lung conditions. For example, although the difference in total DF between static and elastic TWL models is negligible in mild COPD (see Fig. 9), noticeable difference exists between the regional DFs predicted by static and elastic TWL models. Specifically, for mild COPD condition, the static TWL model predicted higher $DF_{MT\text{-}G7}$ for particles with $0.1\,\mu m \le d_p \le 5\,\mu m$ [see Figs. 10(a)–10(f)]. However, the higher $DF_{MT\text{-}G7}$ is balanced by lower $DF_{G8\text{-}acinus}$. For severe COPD condition, since the same deformation kinematics was prescribed for the conducting airways (trachea to G17), the effect of secondary flow induced by airway deformation on the particle interceptions with airway wall is stronger than the effect in mild COPD condition (higher flow rate compared to severe COPD case). This higher intensity of secondary flow in the TB tree leads to higher regional DF in both G1–G7 and G8-acinus regions in the elastic TWL model under severe COPD condition than static case. Thus, the balance existed in total DF between static and elastic cases for mild COPD condition is broken under severe COPD condition as the elastic TWL model predicts higher total DF than the static TWL model for particles with $0.1\,\mu m \le d_p \le 5\,\mu m$. For normal COPD case, the difference in total DF is obvious for small particles ($d_p = 0.1\,\mu m$) and large particles ($d_p = 5$ and $10\,\mu m$). Specifically, for the normal lung condition, static model predicts higher total DF for small particles ($d_p = 0.1\,\mu m$) compared with elastic case mainly because of the Brownian motion effect in G1–G7 region, while the Brownian motion induced deposition is reduced in the elastic TWL model due to airway expansion. For large particles ($d_p = 5$ and $10\,\mu m$), it seems that although the inertia induced deposition in MT is reduced in the elastic TWL case, it predicts much higher $DF_{G8\text{-}acinus}$ resulted from the inertia and higher intensity due to the airway deformation induced secondary flow compared with the static TWL case, which leads to the higher total DF in elastic cases for normal COPD case than the static TWL case.

E. Effect of COPD disease condition on regional deposition fraction

To enhance the delivery dosage of the drugs to the designated lung sites and the treatment effectiveness, the effect of disease-specific airway deformation on regional DF is predicted using the elastic TWL model shown in Figs. 11(a)–11(c), with the focus on the DF in the region from G8 to acinus ($DF_{G8\text{-}acinus}$). For all three lung conditions, the DFs of particles with $0.1 \le d_p \le 10\,\mu m$ in MT are less than 1%. Moreover, particles with $d_p = 5\,\mu m$ have the highest $DF_{G8\text{-}acinus}$. With the increase in particle size, the $DF_{G8\text{-}acinus}$ first decreases (until $d_p = 0.5\,\mu m$) and then increases (until $d_p = 5\,\mu m$). In addition, $DF_{G8\text{-}acinus}$ of $5\,\mu m$ particles is higher than the $DF_{G8\text{-}acinus}$ of $10\,\mu m$ particles. A similar $DF_{G8\text{-}acinus}$ vs d_p trend was predicted in the previous research investigating the deep lung simulation.[14] For the normal lung condition [see Fig. 11(a)], $DF_{G8\text{-}acinus}$ of particles with $d_p = 0.1\,\mu m$ is 17.1%. For particle size in $0.2 \le d_p \le 2\,\mu m$, the $DF_{G8\text{-}acinus}$ is approximately 6%. However, $DF_{G8\text{-}acinus}$ increases dramatically to 54.6% for particles with $d_p = 5\,\mu m$. A similar trend can be observed for mild and severe COPD conditions [see Figs. 11(b) and 11(c)] although for the severe COPD condition as shown in Fig. 11(c), the highest $DF_{G8\text{-}acinus}$ is only 30.4% (when $d_p = 5\,\mu m$). It can be observed that, with the exacerbation in COPD disease condition, i.e., from healthy to severe COPD, the highest delivery efficiency of the inhaled

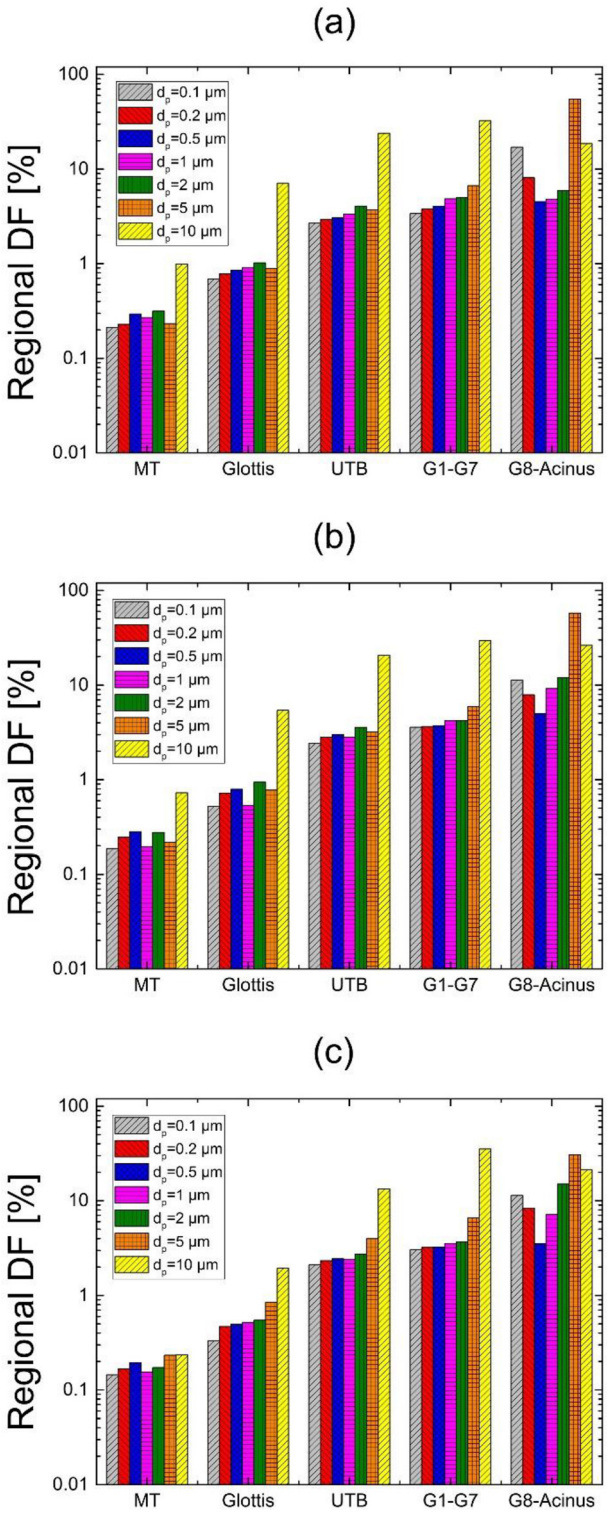

FIG. 11. Comparison of regional DFs predicted via elastic TWL model under different lung disease conditions: (a) normal healthy, (b) mild COPD, and (c) severe COPD.

drug particles decreases which indicates that delivering aerosolized medications to small airways to treat COPD is more challenging for patients with severe disease condition. Such a phenomenon is due to the lack of airway expansion and contraction capability, which results in the additional difficulty to draw the inhaled particles into the deeper airway region. Considering that better treatment for COPD can be achieved as higher drug dosage is delivered into deep airways (after G8), both small (e.g., $d_p = 0.1$ μm) and large particles (e.g., $d_p = 5$ and 10 μm) are favored.

V. CONCLUSIONS

This study developed an innovative elastic truncated whole-lung (TWL) model, covering the entire conductive and respiratory zones of the human pulmonary system, including alveoli, with calibrated airway deformation kinematics for different COPD disease conditions (please see the animation shown in Fig. 12 (Multimedia view) showing particle transport and deposition in the elastic TWL model). The effect of disease-specific airway deformation kinematics on pulmonary air-particle transport dynamics and deposition has been quantified. The results of the delivery efficacy calculated through numerical simulation will assist the determination and optimization of the drug delivery strategy and particle engineering process. The following conclusions can be drawn from the results of the elastic TWL model simulations:

(1) The airway deformation has an apparent influence on the airflow structure in the respiratory system from the glottis to the trachea for the three lung conditions investigated in this work. The effect of airway deformation on airflow structure becomes more evident after the main bronchus.
(2) With increasing particle size from 0.1 to 10 μm, both static and elastic models predict parabolic curves for total DF. However, the regional DFs predicted by static and the elastic whole-lung models are different as higher DF (particle size in 0.1 μm $\leq d_p \leq$ 10 μm) in lower airways is observed in the results from the elastic truncated whole-lung model.
(3) With the exacerbation in COPD disease condition, the highest delivery efficiency of the inhaled drug particles decreases which indicates that delivering aerosolized medications to small airways to treat COPD is more challenging for patients with severe disease condition.
(4) For the particle sizes investigated in this work, $d_p = 5$ μm is recommended as the optimal size of drug particle for all three lung conditions investigated in this study since it gives the highest $DF_{G8\text{-}acinus}$ based on elastic TWL model results.

All above-mentioned conclusions indicate that the disease-specific airway deformation kinematics can significantly influence the predictions of pulmonary air-particle flow dynamics. Therefore, it is necessary to model the airway deformation simultaneously with the tracking of particle-laden airflows in human respiratory system on a disease-specific level in order to either accurately predict the drug delivery efficiency to designated lung sites or assess the occupational exposure health risks based on the lung dosimetry of the inhaled toxicants.

VI. LIMITATIONS OF THE STUDY AND FUTURE WORK

As the limitations of this study, assumptions and simplifications in the elastic TWL model are summarized as follows:

(1) In this study, only one idealized upper airway geometry was employed, which neglects the inter-subject variability effect.[4]
(2) For the study of diseased airway deformation kinematics, the residual volumes (RVs) are assumed to be the same among different lung disease conditions.
(3) Drug particles are assumed to be solid particles with constant diameters, without hygroscopic growth in the humid lung environments.
(4) The airway after G3 is assumed to be symmetrical as the first step for the fundamental study of how airway deformation kinematics can influence the air-particle flow dynamics in human respiratory systems. However, asymmetrical structures widely exist in subject-specific human respiratory systems, may lead to airflow patterns the particle transport phenomena compared with symmetric structures.

To address the limitations of the study listed above, future work include the following:

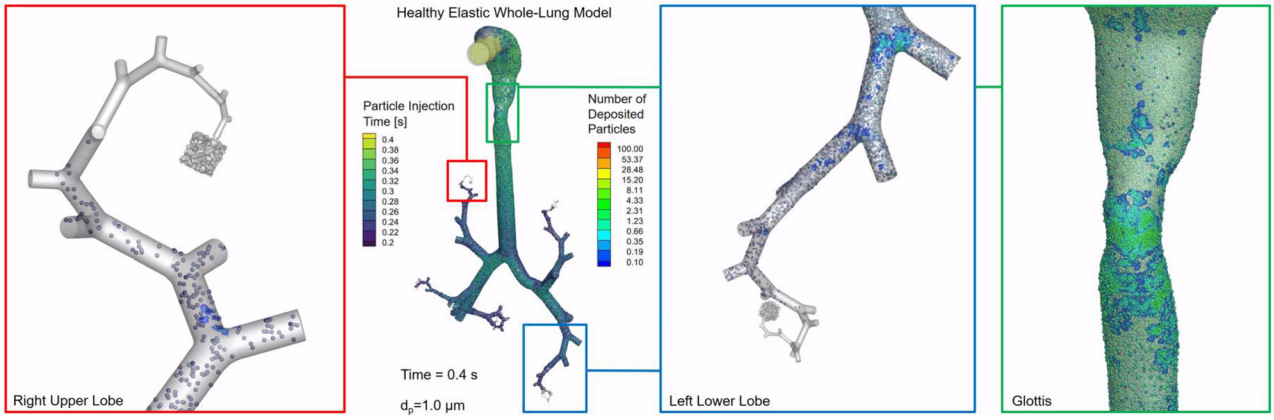

FIG. 12. Animation showing 1-μM particle transport and deposition in the elastic TWL model with physiologically realistic airway deformation for a healthy lung. Multimedia view: https://doi.org/10.1063/5.0065309.1

(1) To investigate the intersubject variability, more elastic TWL geometries can be constructed using subject-specific mouth/nose-to-throat geometries with asymmetrical bifurcating structures.[4]
(2) To simulate more physiologically realistic lung disease conditions, diffeerent residual volume (RV) for different COPD stages and other lung disease conditions will be calibrated and integrated into the elastic TWL modeling framework.[65–67]
(3) The condensation/evaporation induced particle size change dynamics[69,70] in the human respiratory systems will be integrated into the next-gneeration elastic TWL modeling framework.
(4) A whole-lung model with the feature of real anatomy will be constructed in our future research to investigate the effect of intersubject variabilities in airway anatomy after G3 on the airflow pattern and particle transport in the human respiratory system.

SUPPLEMENTARY MATERIAL

See the supplementary material for the complete mesh independence test for the 3 D elastic TWL model.

ACKNOWLEDGMENTS

This material is based upon work supported by the National Science Foundation under Grant No. CBET 2120688. The research was made possible by funding through the award for Project No. HR19–106, from the Oklahoma Center for the Advancement of Science and Technology (OCAST). The use of Ansys software (Ansys Inc., Canonsburg, PA) as part of the Ansys-CBBL academic partnership is also gratefully acknowledged (Dr. Thierry Marchal). This work used resources services and support provided via the COVID-19 HPC Consortium (https://covid19-hpc-consortium.org/), a unique private-public effort to bring together government, industry, and academic leaders who are volunteering free compute time and resources in support of COVID-19 research. Some computational jobs were performed at the High-Performance Computing Center, Oklahoma State University, supported, in part, through the National Science Foundation (Grant No. OAC-1531128).

DATA AVAILABILITY

The data that support the findings of this study are available from the corresponding author upon request.

REFERENCES

[1]N. R. Labiris and M. B. Dolovich, "Pulmonary drug delivery. Part I: Physiological factors affecting therapeutic effectiveness of aerosolized medications," Br. J. Clin. Pharmacol. **56**(6), 588–599 (2003).
[2]Y. Feng, J. Zhao, X. Chen, and J. Lin, "An *in silico* subject-variability study of upper airway morphological influence on the airflow regime in a tracheobronchial tree," Bioengineering **4**(4), 90 (2017).
[3]J. F. Zhao, Y. Feng, and C. A. Fromen, "Glottis motion effects on the inhaled particle transport and deposition in a subject-specific mouth-to-trachea model: An CFPD study," Comput. Biol. Med. **116**, 103532 (2020).
[4]Y. Feng, J. Zhao, C. Kleinstreuer, Q. Wang, J. Wang, D. H. Wu, and J. Lin, "An *in silico* inter-subject variability study of extra-thoracic morphology effects on inhaled particle transport and deposition," J. Aerosol Sci. **123**, 185 (2018).
[5]Y. Feng, C. Kleinstreuer, N. Castro, and A. Rostami, "Computational transport, phase change and deposition analysis of inhaled multicomponent droplet–vapor mixtures in an idealized human upper lung model," J. Aerosol Sci. **96**, 96–123 (2016).
[6]Y. Feng, C. Kleinstreuer, and A. Rostami, "Evaporation and condensation of multicomponent electronic cigarette droplets and conventional cigarette smoke particles in an idealized G3–G6 triple bifurcating unit," J. Aerosol Sci. **80**, 58–74 (2015).
[7]P. Koullapis, S. C. Kassinos, J. Muela, C. Perez-Segarra, J. Rigola, O. Lehmkuhl, Y. Cui, M. Sommerfeld, J. Elcner, M. Jicha, I. Saveljic, N. Filipovic, F. Lizal, and L. Nicolaou, "Regional aerosol deposition in the human airways: The SimInhale benchmark case and a critical assessment of *in silico* methods," Eur. J. Pharm. Sci. **113**, 77–94 (2018).
[8]P. G. Koullapis, L. Nicolaou, and S. C. Kassinos, "In silico assessment of mouth-throat effects on regional deposition in the upper tracheobronchial airways," J. Aerosol Sci. **117**, 164–188 (2018).
[9]M. S. Islam, S. C. Saha, E. Sauret, T. Gemci, and Y. T. Gu, "Pulmonary aerosol transport and deposition analysis in upper 17 generations of the human respiratory tract," J. Aerosol Sci. **108**, 29–43 (2017).
[10]M. S. Islam, S. C. Saha, T. Gemci, I. A. Yang, E. Sauret, Z. Ristovski, and Y. T. Gu, "Euler-Lagrange prediction of diesel-exhaust polydisperse particle transport and deposition in lung: Anatomy and turbulence effects," Sci. Rep. **9**(1), 12423 (2019).
[11]S. Newman, W. D. Bennett, M. Biddiscombe, S. G. Devadason, M. B. Dolovich, J. Fleming, S. Haeussermann, C. Kietzig, P. J. Kuehl, B. L. Laube, K. Sommerer, G. Taylor, O. S. Usmani, and K. L. Zeman, "Standardization of techniques for using planar (2D) imaging for aerosol deposition assessment of orally inhaled products," J. Aerosol Med. Pulm. Drug Delivery **25**(S1), S10–S28 (2012).
[12]J. Conway, J. Fleming, M. Bennett, and T. Havelock, "The co-imaging of gamma camera measurements of aerosol deposition and respiratory anatomy," J. Aerosol Med. Pulm. Drug Delivery **26**(3), 123–130 (2013).
[13]A. V. Kolanjiyil and C. Kleinstreuer, "Computational analysis of aerosol-dynamics in a human whole-lung airway model," J. Aerosol Sci. **114**, 301–316 (2017).
[14]P. G. Koullapis, F. S. Stylianou, J. Sznitman, B. Olsson, and S. C. Kassinos, "Towards whole-lung simulations of aerosol deposition: A model of the deep lung," J. Aerosol Sci. **144**, 105541 (2020).
[15]K. Poorbahrami, I. E. Vignon-Clementel, S. C. Shadden, and J. M. Oakes, "A whole lung in silico model to estimate age dependent particle dosimetry," Sci. Rep. **11**(1), 11180 (2021).
[16]P. W. Longest, G. Tian, N. Khajeh-Hosseini-Dalasm, and M. Hindle, "Validating whole-airway CFD predictions of DPI aerosol deposition at multiple flow rates," J. Aerosol Med. Pulm. Drug Delivery **29**(6), 461–481 (2016).
[17]Y. Yin, J. Choi, E. A. Hoffman, M. H. Tawhai, and C.-L. Lin, "A multiscale MDCT image-based breathing lung model with time-varying regional ventilation," J. Comput. Phys. **244**, 168–192 (2013).
[18]Z. Zhang, C. Kleinstreuer, and C. S. Kim, "Airflow and nanoparticle deposition in a 16-generation tracheobronchial airway model," Ann. Biomed. Eng. **36**(19), 2095–2110 (2008).
[19]Taulbee, D. B. and C. P. Yu, "A theory of aerosol deposition in the humen respirtory tract," J. Appl. Physiol. **38**(1), 77–85 (1975).
[20]A. V. Kolanjiyil and C. Kleinstreuer, "Computationally efficient analysis of particle transport and deposition in a human whole-lung-airway model. Part I: Theory and model validation," Comput. Biol. Med. **79**, 193–204 (2016).
[21]D. Hasler, P. Anagnostopoulou, S. Nyilas, P. Latzin, J. Schittny, and D. Obrist, "A multi-scale model of gas transport in the lung to study heterogeneous lung ventilation during the multiple-breath washout test," PLoS Comput. Biol. **15**(6), e1007079 (2019).
[22]X. Cui, W. Wu, and H. Ge, "Investigation of airflow field in the upper airway under unsteady respiration pattern using large eddy simulation method," Respir. Physiol. Neurobiol. **279**, 103468 (2020).
[23]A. F. Tena, J. Fernández, E. Álvarez, P. Casan, and D. K. Walters, "Design of a numerical model of lung by means of a special boundary condition in the truncated branches," Int. J. Numer. Meth. Biomed. Eng. **33**(6), e2830 (2017).
[24]M. H. Tawhai, A. Pullan, and P. Hunter, "Generation of an anatomically based three-dimensional model of the conducting airways," Ann. Biomed. Eng. **28**(7), 793–802 (2000).

[25]A. Pandal-Blanco, R. Barrio-Perotti, R. Agujetas-Ortiz, and A. Fernández-Tena, "Implementation of a specific boundary condition for a simplified symmetric single-path CFD lung model with OpenFOAM," Biomech. Model. Mechanobiol. **18**(6), 1759–1771 (2019).
[26]A. Fernández-Tena, R. Barrio-Perotti, E. Blanco-Marigorta, and A. Pandal-Blanco, "*In silico* prototype of a human lung with a single airway to predict particle deposition," Int. J. Numer. Methods Biomed. Eng. **36**(6), e3339 (2020).
[27]X. April Si, M. Talaat, and J. Xi, "SARS COV-2 virus-laden droplets coughed from deep lungs: Numerical quantification in a single-path whole respiratory tract geometry," Phys. Fluids **33**(2), 023306 (2021).
[28]G. Tian, P. W. Longest, G. Su, R. L. Walenga, and M. Hindle, "Development of a stochastic individual path (SIP) model for predicting the tracheobronchial deposition of pharmaceutical aerosols: Effects of transient inhalation and sampling the airways," J. Aerosol Sci. **42**(11), 781–799 (2011).
[29]A. Dutta, *Numerical Simulation of the Air Flow and Particulate Deposition in Emphysematous Human Acini* (University of British Columbia, 2016).
[30]J. Xi, Z. Wang, K. Talaat, C. Glide-Hurst, and H. Dong, "Numerical study of dynamic glottis and tidal breathing on respiratory sounds in a human upper airway model," Sleep Breathing **22**(2), 463–479 (2018).
[31]J. H. Kang, J. Choi, K. J. Chae, K. M. Shin, C.-H. Lee, J. Guo, C.-L. Lin, E. A. Hoffman, and C. Lee, "CT-derived 3D-diaphragm motion in emphysema and IPF compared to normal subjects," Sci. Rep. **11**(1), 14923 (2021).
[32]A. De Boer, P. Hagedoorn, M. Hoppentocht, F. Buttini, F. Grasmeijer, and H. Frijlink, "Dry powder inhalation: Past, present and future," Expert Opin. Drug Delivery **14**(4), 499–512 (2017).
[33]B. Sul, T. Altes, K. Ruppert, K. Qing, D. S. Hariprasad, M. Morris, J. Reifman, and A. Wallqvist, "Dynamics of the tracheal airway and its influences on respiratory airflows: An exemplar study," J. Biomech. Eng. **141**(11), 111009 (2019).
[34]R. Werner, J. Ehrhardt, R. Schmidt, and H. Handels, "Modeling respiratory lung motion: A Biophysical approach using finite element methods," Proc. SPIE **6916**, 69160N (2008).
[35]P. Aghasafari and R. Pidaparti, "Influence of tidal-volume setting, emphysema and ARDS on human alveolar sacs mechanics," Acta Mech. Sin. **34**(5), 983–993 (2018).
[36]B. Seyfi, A. P. Santhanam, and O. J. Ilegbusi, "A biomechanical model of human lung deformation utilizing patient-specific elastic property," J. Cancer Therapy **7**(6), 402–415 (2016).
[37]B. Seyfi Noferest, A. P. Santhanam, and O. J. Ilegbusi, "Effect of gravity on subject-specific human lung deformation," Math. Comput. Modell. Dyn. Syst. **24**(1), 87–101 (2018).
[38]J. Xi, K. Talaat, and X. A. Si, "Deposition of bolus and continuously inhaled aerosols in rhythmically moving terminal alveoli," J. Comput. Multiphase Flows **10**(4), 178–193 (2018).
[39]A. Comerford, C. Forster, and W. A. Wall, "Structured tree impedence outflow boundary conditions for 3D lung simulations," J. Biomech. Eng. **132**, 081002 (2010).
[40]W. A. Wall and T. Rabczuk, "Fluid–structure interaction in lower airways of CT-based lung geometries," Int. J. Numer. Methods Fluids **57**(5), 653–675 (2008).
[41]M. Malvè, A. Pérez del Palomar, S. Chandra, J. López-Villalobos, A. Mena, E. Finol, A. Ginel, and M. Doblaré, "FSI analysis of a healthy and a stenotic human trachea under impedance-based boundary conditions," J. Biomech. Eng. **133**(2), 021001 (2011).
[42]K. Talaat and J. Xi, "Computational modeling of aerosol transport, dispersion, and deposition in rhythmically expanding and contracting terminal alveoli," J. Aerosol Sci. **112**, 19–33 (2017).
[43]G. Xia, M. H. Tawhai, E. A. Hoffman, and C.-L. Lin, "Airway wall stiffening increases peak wall shear stress: A fluid–structure interaction study in rigid and compliant airways," Ann. Biomed. Eng. **38**(5), 1836–1853 (2010).
[44]D. R. Subramaniam, G. Mylavarapu, R. J. Fleck, R. S. Amin, S. R. Shott, and E. J. Gutmark, "Effect of airflow and material models on tissue displacement for surgical planning of pharyngeal airways in pediatric down syndrome patients," J. Mech. Behav. Biomed. Mater. **71**, 122–135 (2017).
[45]P. Hofemeier and J. Sznitman, "The role of anisotropic expansion for pulmonary acinar aerosol deposition," J. Biomech. **49**(14), 3543–3548 (2016).
[46]J. Wang, J. Xi, P. Han, N. Wongwiset, J. Pontius, and H. Dong, "Computational analysis of a flapping uvula on aerodynamics and pharyngeal wall collapsibility in sleep apnea," J. Biomech. **94**, 88–98 (2019).
[47]J. Feher, "Lung volumes and airway resistance," in *Quantitative Human Physiology*, 2nd Edition), edited by J. Feher (Academic Press, Boston, 2017), pp 633–641.
[48]A. Chandel, A. K. Goyal, G. Ghosh, and G. Rath, "Recent advances in aerosolised drug delivery," Biomed. Pharmacother. **112**, 108601 (2019).
[49]J. Xi and P. W. Longest, "Transport and deposition of micro-aerosols in realistic and simplified models of the oral airway," Ann. Biomed. Eng. **35**(4), 560–581 (2007).
[50]ICRP, "Human respiratory tract model for radiological protection," Ann. ICRP, Publ. **24**(1–3), 125 (1994).
[51]C. S. Wang, "Inhaled Particles," Interface Sci. Technol. **5**, 1–187 (2005).
[52]K. Koshiyama and S. Wada, "Mathematical model of a heterogeneous pulmonary acinus structure," Comput. Biol. Med. **62**, 25–32 (2015).
[53]J. Xi, M. Talaat, H. Tanbour, and K. Talaat, "Airflow and particle deposition in acinar models with interalveolar septal walls and different alveolar numbers," Comput. Math Methods Med. **2018**, 3649391.
[54]C. Plathow, S. Ley, C. Fink, M. Puderbach, M. Heilmann, I. Zuna, and H.-U. Kauczor, "Evaluation of chest motion and volumetry during the breathing cycle by dynamic MRI in healthy subjects," Invest. Radiol. **39**, 202–209 (2004).
[55]Y. Feng and C. Kleinstreuer, "Analysis of non-spherical particle transport complex internal shear flows," Phys. Fluids **25**, 01904 (2013).
[56]Z. Zhang, C. Kleinstreuer, and S. Hyun, "Size-change and deposition of conventional and composite cigarette smoke particles during inhalation in a subject-specific airway model," J. Aerosol Sci. **46**, 34–52 (2012).
[57]Z. Zhang, C. Kleinstreuer, and Y. Feng, "Vapor deposition during cigarette smoke inhalation in a subject-specific human airway model," J. Aerosol Sci. **53**, 40–60 (2012).
[58]G. Tian, M. Hindle, S. Lee, and P. W. Longest, "Validating CFD predictions of pharmaceutical aerosol deposition with in vivo data," Pharm. Res. **32**(10), 3170–3187 (2015).
[59]"Respiratory physiology," in *Basic Physiology for Anaesthetists*, 2nd ed. edited by C. Huang, D. Chambers, and G. Matthews (Cambridge University Press, Cambridge, 2019), pp. 50–55.
[60]J. E. Hall, "Pulmonary ventilation," in *Guyton and Hall Textbook of Medical Physiology*, 13th ed. (Elsevier Health Sciences, London, 2015).
[61]J. Mead, J. M. Turner, and J. B. Little, "Significance of the relationship between lung recoil and maximum expiratory flow," J. Appl. Physiol. **22**(1), 95–108 (1967).
[62]R. L. Walenga, G. Tian, and P. Worth Longest, "Development of characteristic upper tracheobronchial airway models for testing pharmaceutical aerosol delivery," J. Biomech. Eng. **135**(9), 91010 (2013).
[63]J. Xi, J. E. Yuan, M. Yang, X. Si, Y. Zhou, and Y.-S. Cheng, "Parametric study on mouth–throat geometrical factors on deposition of orally inhaled aerosols," J. Aerosol Sci. **99**, 94–106 (2016).
[64]W. Stahlhofen, G. Rudolf, and A. C. James, "Intercomparison of experimental regional aerosol deposition data," J. Aerosol Med. **2**(3), 285–308 (1989).
[65]G. T. Ferguson, "Why Does the Lung Hyperinflate?," Proc. Am. Thorac. Soc. **3**(2), 176–179 (2006).
[66]P. Biselli, P. R. Grossman, J. P. Kirkness, S. P. Patil, P. L. Smith, A. R. Schwartz, and H. Schneider, "The effect of increased lung volume in chronic obstructive pulmonary disease on upper airway obstruction during sleep," J. Appl. Physiol. **119**(3), 266–271 (2015).
[67]S. Scarlata, L. Paladini, M. Cesari, and R. A. Incalzi, "Lung volumes in COPD: Not only the total lung capacity," Chest **138**(1), 233 (2010).
[68]X. Chen, Y. Feng, W. Zhong, and C. Kleinstreuer, "Numerical investigation of the interaction, transport and deposition of multicomponent droplets in a simple mouth-throat model," J. Aerosol Sci. **105**, 108–127 (2017).
[69]T. Manzoor, F. Muneer, M. Ibrahim, S. Tahira, and R. Azmat, "Effectiveness of voice therapy in dysphonia: A speech-pathologist perspective," B.Sc thesis (Hons) SLP (Department of Allied Health Sciences FMH College of Medicine & Dentistry, Shadman Lahore, 2015).
[70]The Mechanics of Human Breathing, see https://courses.lumenlearning.com/boundless-biology/chapter/breathing/ (last accessed June 30, 2021).